Journal of Materials Chemistry C

Effect of *Ortho*-Fluorine Substituted Hole Transport Materials for Perovskite Solar Cells: Influence of Rigid vs. Flexible Linkers

Journal:	*Journal of Materials Chemistry C*
Manuscript ID	TC-ART-04-2025-001565.R1
Article Type:	Paper
Date Submitted by the Author:	04-Jun-2025
Complete List of Authors:	Raju, Telugu; Kyushu University International Institute for Carbon-neutral Energy Research Senevirathne, Chathuranganie; Kyushu University International Institute for Carbon-neutral Energy Research Watanabe, Motonori; Kyushu University, International Institute for Carbon-Neutral Energy Research Fujita, Yuki; Kyushu University Senba, Dai; Kyushu University Matsushima, Toshinori; Kyushu University, International Institute for Carbon-Neutral Energy Research

ARTICLE

Effect of *Ortho*-Fluorine Substituted Hole Transport Materials for Perovskite Solar Cells: Influence of Rigid vs. Flexible Linkers

Received 00th January 20xx,
Accepted 00th January 20xx

DOI: 10.1039/x0xx00000x

Telugu Bhim Raju,[a]* Chathuranganie A. M. Senevirathne,[a] Motonori Watanabe,[abcd] Yuki Fujita,[ab] Dai Senba,[ac] Toshinori Matsushima*[abcd]

The development of stable and efficient hole transporting materials (HTMs) is essential for the commercialization of perovskite solar cells (PSCs). In this study, we introduce four novel HTMs featuring a D-π-D molecular structure. These HTMs have 3-fluoro-*N,N*-bis(4-(methylthio)phenyl)aniline (TPASF) peripheral terminal groups, which are linked with various π-core moieties. Our investigation reveals that altering the π-linkers affects the film morphology of the HTMs, significantly influencing device performance. HTMs with planar backbones, CPDT-OFTPASMe2 [2-(2,6-bis(4-(bis(4-(methylthio)phenyl)amino)-2-fluorophenyl)-4*H*-cyclopenta[2,1-*b*:3,4-*b'*]dithiophen-4-ylidene)malononitrile] and TTT-OFTPASMe2 [4,4'-(dithieno[3,2-*b*:2',3'-*d*]thiophene-2,6-diyl)bis(3-fluoro-*N,N*-bis(4-(methylthio)phenyl)aniline)], form films with more voids. In contrast, ThOEt-OFTPASMe2 [4,4'-(3,3'-diethoxy-[2,2'-bithiophene]-5,5'-diyl)bis(3-fluoro-*N,N*-bis(4-(methylthio)phenyl)aniline)] and DTP-OFTPASMe2 [4,4'-(4-(4-methoxyphenyl)-4*H*-dithieno[3,2-*b*:2',3'-*d*]pyrrole-2,6-diyl)bis(3-fluoro-*N,N*-bis(4-(methylthio)phenyl)aniline)], with inhibitory effects caused by ethoxy and methoxy phenyl groups, respectively, prevent film aggregation and result in a pinhole-free morphology. Among the four HTMs, the fresh device with DTP-OFTPASMe2 HTM emerges as particularly promising, exhibiting an average power conversion efficiency of 18.77% and good thermal stability. Subsequent at amibient condition to promote oxidation boosts the efficiency to 21.35% in unsealed devices. Furthermore, air-exposed DTP-OFTPASMe2-based devices maintain their initial efficiency under high-humidity conditions for approximately 83 days, underscoring their robust performance over time.

1 Introduction

Power conversion efficiencies (PCEs) of perovskite solar cells (PSCs) have significantly improved from 3.83% to over 27% in single-junction architectures and 34.9% in perovskite/silicon tandem architectures.[1] This remarkable progress is attributed to the superior properties of perovskites, such as high absorption coefficients, high charge carrier mobility, long charge carrier diffusion lengths, and compatibility with solution processing, among others.[2,3] These characteristics highlight the immense potential of PSCs as a low-cost renewable energy source to meet increasing global energy demands. However, achieving PSCs with sufficient durability for real-world power generation remains a critical challenge before commercialization. The design and formulation of the hole-transporting material (HTM) layer play a pivotal role in addressing these durability and stability issues.

The HTMs facilitate hole extraction and electron blocking, making them crucial components for achieving high efficiency and stability in PSCs. Inorganic, organic small-molecule, and polymeric HTMs have been developed for this purpose. However, inorganic HTMs often require high-temperature processing (>200 °C), and polymeric HTMs are typically challenging to purify.[4] As a result, significant research attention has been focused on organic small-molecule HTMs.[5–10] Ideal HTMs should possess suitable energy levels, excellent hole conductivity, good solubility in organic solvents, high chemical, photothermal, and morphological stability, along with cost-effective and straightforward synthesis. To meet these criteria, most HTMs are designed with a linear π-conjugated core that enables favorable intermolecular π-π interactions, leading to compact molecular packing in films. This, in turn, facilitates efficient hole transport and extraction at the interface with the perovskite light absorber.[10] Numerous HTMs based on pyrene,[11,12] indacenodithiophene,[13,14] anthanthrone,[15] tetrathienylethene,[16] tetrathienoanthracene,[17] and thiophene-fused molecular backbones such as dithieno[3,2-*b*:2',3'-*d*]pyrrole,[18–24] tetrathienopyrrole,[25] benzo[1,2-*b*:4,5-*b'*]dithiophene,[20,26] benzo[1,2-*b*:3,4-*b'*:5,6-*b'*]trithiophene,[27]

[a] *International Institute for Carbon-Neutral Energy Research (WPI-I2CNER), Kyushu University, Fukuoka 819-0395, Japan. E-mail: tmatusim@i2cner.kyushu-u.ac.jp*
[b] *Department of Applied Chemistry, Faculty of Engineering, Kyushu University, Fukuoka 819-0395, Japan.*
[c] *Department of Automotive Science, Graduates School of Integrated Frontier Sciences, Kyushu University, 744 Motooka, Nishi, Fukuoka 819-0395, Japan*
[d] *Center for Energy Systems Design (CESD), International Institute for Carbon-Neutral Energy Research (WPI-I2CNER), Kyushu University, Fukuoka 819-0395, Japan*

† Electronic supplementary information (ESI) available. See DOI:

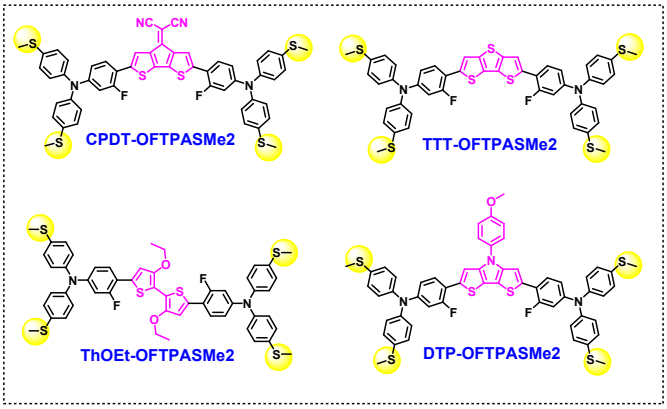

Fig. 1 Chemical structures of the newly developed HTMs.

phenanthrene,[28,29] quinoxaline,[30,31] and phenanthroline,[32] have been reported. These HTMs often incorporate donor units like triphenylamine (TPA) or 4-methoxy-*N*-(4-methoxyphenyl)-*N*-phenylaniline (MeOTPA).[9] Thiophene-fused heterocycles have shown particularly promising photovoltaic performance due to their excellent optoelectronic properties, strong intermolecular interactions (S···S, S···π), and their potential to passivate perovskite defects through S-Pb^{+2} interactions. [18,20,21,33]

In many HTMs, methoxy (MeO) groups are introduced as they facilitate oxidation, resulting in high hole conduction. Additionally, MeO groups enhance molecular interactions with the perovskite's methylammonium, creating an efficient hole-transfer pathway.[34] However, MeO groups have notable drawbacks. Their strong electron-donating properties lower the oxidation potential of HTMs, which can result in a reduction of the open-circuit voltage (*V*oc).[35] Furthermore, the *p*-anisole structure in MeOTPA contributes to significant degradation of PSCs at elevated temperatures due to its limited glass transition temperature (T_g). Moreover, MeO groups in MeOTPA increase the hydrophilicity of the HTM layer, negatively impacting device stability.[35] Thus, MeO groups present a trade-off between efficiency and stability.[36–39] Despite this, methoxy-free arylamines that outperform MeOTPA in terms of efficiency and stability have been scarcely reported.[40–42] Replacing MeO groups with methylthio (MeS) groups offers a promising alternative, as the MeS group exhibits a pπ(C)–dπ(S) orbital overlap, where sulfur accepts π-electrons from the π-orbitals of C=C bonds into its empty 3*d* orbitals. This modification has the potential to address the limitations of MeO groups effectively.

On the other hand, high carrier mobility of HTMs is crucial for improving PCE. To enhance mobility, achieving denser molecular packing through self-assembly via intermolecular noncovalent interactions is an effective strategy.[34] Fluorine (F) substitution in organic HTMs can promote strong intermolecular noncovalent interactions, which contribute to enhanced molecular packing. Additionally, F substitution provides moisture resistance, especially in conventional device architectures where the top HTM layer protects the perovskite layer.[43] Moreover, F substitution is an effective approach to tuning the optoelectronic properties, molecular planarity, and film morphology of HTMs. These enhancements improve intramolecular charge transfer (ICT), leading to increased hole mobility and higher dipole moments in HTMs.[42,43] The incorporation of F substitution into MeOTPA-based HTMs is widely utilized to further boost photovoltaic performance and achieve environmentally stable PSCs.[43–46]

In this work, we introduced F substitution on the phenyl unit of a 3-fluoro-*N,N*-bis(4-(methylthio)phenyl)aniline (TPASF) donor in a D-π-D structured HTM and investigated its impact on device performance and stability. We synthesized four new small-molecule HTMs incorporating different central π-bridge cores: 2-(4*H*-cyclopenta[2,1-*b*:3,4-*b'*]dithiophen-4-ylidene)malononitrile (CPDT), dithieno[3,2-*b*:2',3'-*d*]thiophene (TTT), 3,3'-diethoxy-2,2'-bithiophene (2ThOEt), and 4-(4-methoxyphenyl)-4*H*-dithieno[3,2-*b*:2',3'-*d*]pyrrole (DTP), all linked with the TPASF donor. Figure 1 illustrates the chemical structures of these TPASF-based HTMs, with detailed synthetic routes and characterizations provided in Figure S1 and the Supporting Information. The introduction of bithiophene units (fused or non-fused) as π-spacers extends π-conjugation. The ortho-F substitution results in a more planar structure compared to F substitution on outer methoxyphenyl units.[44,45,47,48-50] These HTMs exhibit multi-molecular dipole-dipole interactions between the core and side groups, such as F (side)-S (core) or F (side)-H (C-H, π) (as discussed later in the crystal structure and Gaussian images), which significantly enhance molecular planarity, intramolecular charge delocalization, and π-π stacking ability. Considering their strong electron-donating ability and excellent hole-transporting capability, the propeller-like TPASF core is employed as peripheral arms. These structures are not only easy to synthesize but may also contribute to reducing charge recombination, mitigating thermal degradation, and minimizing electron coupling in PSCs.

Among the newly developed four HTMs, the DTP-OFTPASMe2 HTM demonstrated significant advantages in PCE, as well as superior air and thermal stability. HTMs with MeS groups exhibit lower oxidation propensity compared to those with methoxy groups at the terminal ends.[45] In this study, chemically doped DTP-OFTPASMe2 HTM achieved an initial average PCE of 18.77% in as-fabricated PSCs. Unsealed DTP-OFTPASMe2 HTM devices reached a maximum PCE of 21.5% after 5 days under ambient conditions, attributed to improve the charge carrier diffusion length of perovskite film and slow oxidation in the HTM layer and oxygen doping, which increased the free hole density. These devices showed an average *V*oc of ~1.11 V, a short-circuit current density (*J*sc) of ~23.7 mA cm^{-2}, a fill factor (FF) of ~76.8%, and a stabilized PCE of ~21.35%. Typically, chemically doped PSCs suffer from low air stability due to the hygroscopic nature of dopants. However, in this case, the fluorine substitution on TPASF effectively prevented moisture penetration and enhanced the molecular backbone's planar conformation. As a result, DTP-OFTPASMe2 HTM devices maintained their initial efficiency for over 83 days under ambient air conditions (relative humidity = 60 ± 5%).

Results and discussion

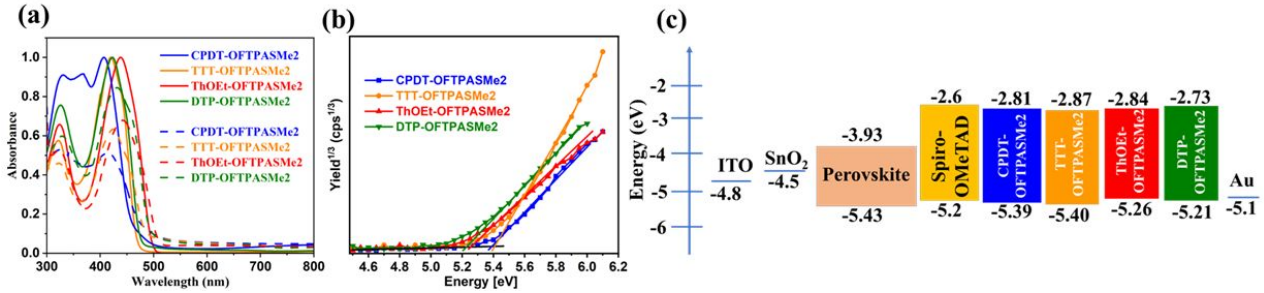

Fig. 2 (a) Normalized UV-Vis-NIR absorption spectra of the HTMs in chloroform solution (solid line) and thin films (dotted line), (b) PYS plots of HTM's solid-state films deposited on ITO substrates, and (c) schematic energy-level diagram of PSCs incorporating the HTMs.

The synthetic routes for the four HTMs are shown in Figure S1, with detailed procedures provided in the Supporting Information. All intermediates, including 3-fluoro-*N,N*-bis(4-(methylthio)phenyl)-4-(4,4,5,5-tetramethyl-1,3,2-dioxaborolan-2-yl)aniline,[46] and dibrominated bithiophene derivatives,[19,48,51,52] were synthesized following established literature methods. The target HTM compounds were obtained through a Suzuki coupling reaction between the corresponding dibrominated bithiophene precursors and 3-fluoro-*N,N*-bis(4-(methylthio)phenyl)-4-(4,4,5,5-tetramethyl-1,3,2-dioxaborolan-2-yl)aniline, catalyzed by $Pd(PPh_3)_4$.[19,48–53] The chemical structures of the synthesized HTMs were fully characterized using proton and carbon nuclear magnetic resonance spectroscopy (^{1}H-NMR and ^{13}C-NMR) and matrix-assisted laser desorption/ionization time-of-flight mass spectrometry (MALDI-TOF/TOF-MS) (see Supporting Information for details).

The ultraviolet-visible-near infrared (UV–VIS-NIR) absorption properties of the undoped HTMs were measured in dilute chloroform solutions and thin films (Figure 2a), with the key parameters summarized in Table 1. All HTMs exhibited two absorption bands in the ranges of 250–350 nm and 350–520 nm. Which is attributed to the π-π* transition and internal charge transfer (ICT), respectively. These strong ICT absorption bands can be ascribed to the intramolecular electron transfer transitions between the central π -core and the terminal TPASF units. In thin films, the absorption spectra of all HTMs showed a slight red shift (≤ 8 nm) compared to their solution states, indicating strong π–π interactions in the solid-state films. Subsequently, photoelectron yield spectroscopy (PYS) was applied to measure the highest occupied molecular orbital (HOMO) with respect to the vacuum level for undoped CPDT, TTT, ThOEt and DTP HTMs thin films (Figure 2b), which were calculated to be −5.39, −5.40, −5.26 and −5.21 eV, respectively. These values nearly match the valence band maximum of the $Cs_{0.05}(FA_{0.85}MA_{0.15})_{0.95}Pb(I_{0.85}Br_{0.15})_3$ perovskite used in subsequent solar cell fabrication (−5.43 eV), facilitating efficient hole extraction from the perovskite to the HTMs (Figure 2c).[54] The lowest unoccupied molecular orbital (LUMO) energy levels, calculated by using formula, (LUMO) = HOMO − optical energy gap (E_g) of the HTMs were estimated to be −2.81 eV (CPDT), −2.87 eV (TTT), −2.84 eV (ThOEt), and −2.73 eV (DTP). These LUMO levels are significantly shallower than the conduction band minimum of the perovskite (−3.93 eV), which effectively prevents electron back-transfer.

Subsequently, density functional theory (DFT) calculations[20] were performed using the B3LYP/6-31(*d,p*) basis set to gain insights into the molecular geometries, frontier molecular orbital (FMO) energy levels, and dipole moments of the four HTMs as shown in Figure 3, delocalization. Moreover, Figure 3 illustrates that the HOMO is distributed across the entire molecule, from the central π-core to the triphenylamine moieties, while the LUMO is primarily localized on

Table 1. Optical and electrochemical properties of the four HTMs.

HTM	Absorption (nm)		ε_{max}		$\lambda_{onset,film}$ (nm)	E_g^{opt} (eV) [c]	Energy level (eV)	
	Solution[a]	Film	Solution (M^{-1} cm^{-1})	Film[b] (cm^{-1})			HOMO[d]	LUMO[e]
CPDT-OFTPASMe2	410, 366	412, 325	14,333	0.51×10^5	480	2.58	−5.39	−2.81
TTT-OFTPASMe2	420, 323	425, 325	11,666	0.64×10^5	490	2.53	−5.40	−2.87
ThOEt-OFTPASMe2	438, 325	442, 325	14,000	0.69×10^5	511	2.42	−5.26	−2.84
DTP- OFTPASMe2	425, 328	432, 330	33,333	0.85×10^5	498	2.48	−5.21	−2.73

[a]*((Absorption spectra measured in chloroform));* [b]*((ε_{max} of thin films fabricated by spin-coating from solutions with 60 mg/mL));* [c]*((The optical bandgap was obtained from $E_g^{opt} = 1240/\lambda_{onset}$));*

[d]*((The HOMO level estimated form PYS).* [e]*((The LUMO level estimated by $E_{HOMO} - E^{opt}_g$))*

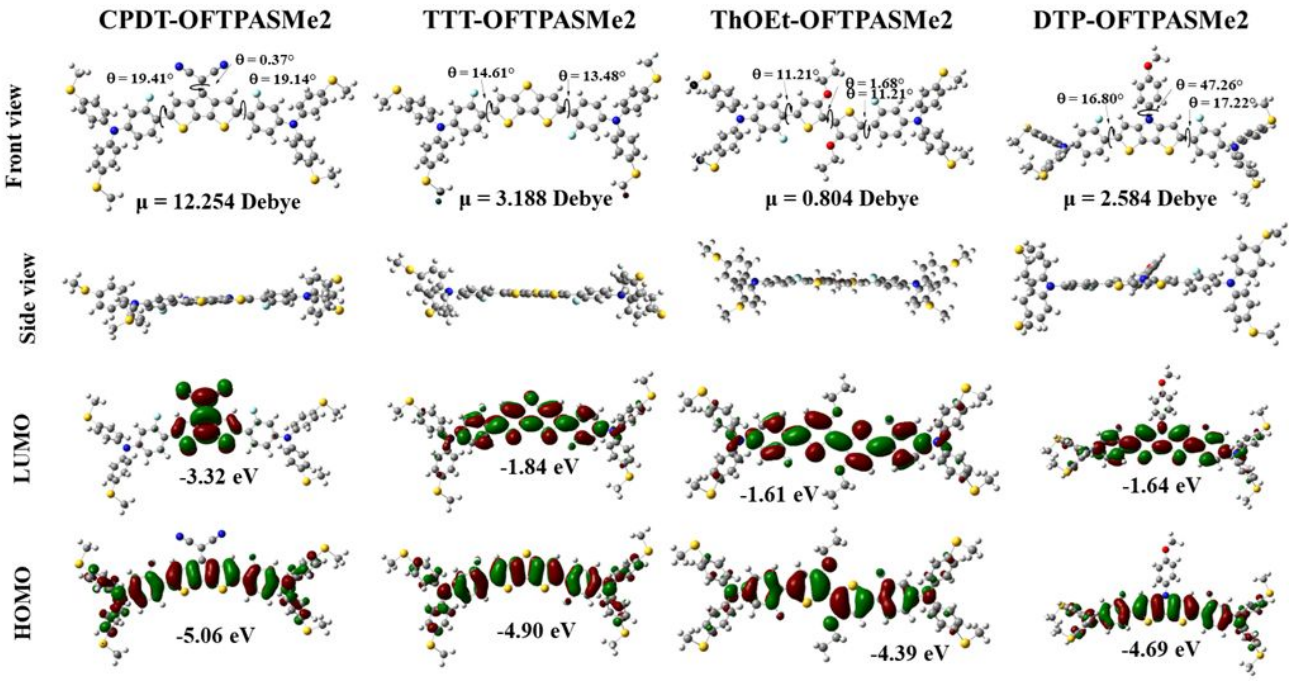

Fig. 3 DFT-optimized molecular configurations of HTMs (top view and side view), dihedral angles, dipole moments, HOMO and LUMO distributions, and energy levels calculated at the B3LYP/6-31G*(d,p)* basis set.

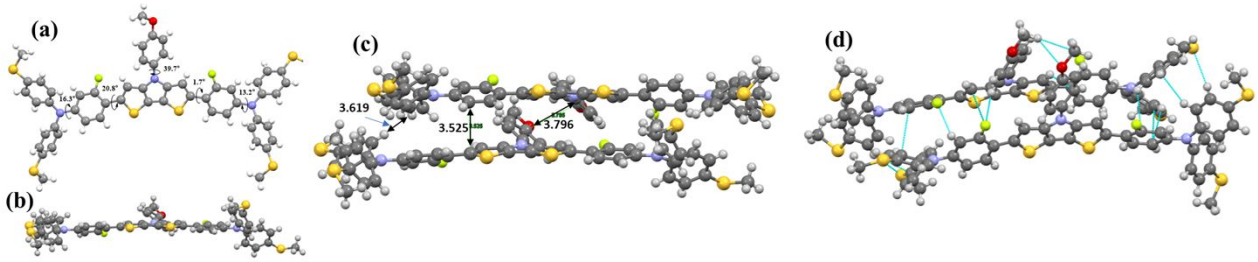

Fig. 4. Single-crystal X-ray structural analysis of DTP-OFTPASMe2. (a) Top-view and (b) side-view molecular geometries, showing the torsion angles between the phenyl rings and the central dithienopyrrole core. (c) Distances between adjacent molecules. (d) Intermolecular interactions, including H–bonding (F−H, O−H, S−H) and C−H/π interactions.

the central π-bridge. The HOMO/LUMO energy levels estimated from DFT calculations are −5.06/−3.32 eV (CPDT), −4.90/−1.84 eV (TTT), −4.39/−1.61 eV (ThOEt), and −4.69/−1.64 eV (DTP). Notably, substituting the central core units with electron-withdrawing cyano groups in CPDT-OFTPASMe2 results in deeper HOMO/LUMO levels.

Additionally, electronic transitions from HOMO to LUMO and other excitations were analyzed, with the computational results presented in Figure S2 and Table S1 (Supporting Information). DFT calculations revealed that the TPASF-based HTMs possess intrinsic molecular dipole moments arising from their structural framework and their ability to form polar molecular arrangements. The high electronegativity and strong electron-withdrawing nature of F enhance the positive character of the triphenylamine moiety, thereby contributing to the overall dipole formation. The central cores CPDT, TTT, ThOEt, and DTP modulate the magnitude of the dipole moment, which in turn influences the interaction between the HTMs and the perovskite layer, ultimately affecting PSC performance. The calculated dipole moments were 12.254 Debye (CPDT), 3.188 Debye (TTT), 0.804 Debye (ThOEt), and 2.584 Debye (DTP).

Single crystals of DTP-OFTPASMe2 were grown by slow evaporation of saturated chloroform/hexane solutions at ambient temperature. X-ray diffraction (XRD) measurements provide crucial insights into the molecular packing motif and intermolecular distances in the solid state. The torsion angles and packing structures of DTP-OFTPASMe2 are presented in Figures 4(a–d). As shown in Figure S3 and Table S2 (Supporting Information), the molecules crystallize in a triclinic $P\bar{1}$ space group with lattice parameters: a = 15.0182(14) Å, b = 15.0957(13) Å, c = 35.0220(3) Å, α = 93.6909(7)°, β = 101.5017(8)°, and γ = 99.7237(8)°. In the DTP HTM, dimers adopt a characteristic slipped π-stacking mode, featuring a face-to-face arrangement within columns and an edge-to-edge arrangement between columns. The face-to-face distance between the central cores of two neighboring molecules is 3.52 Å, while the distances

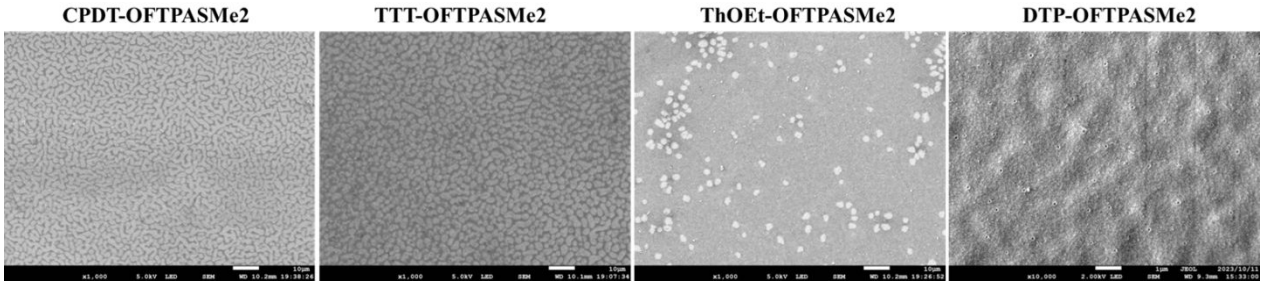

Fig. 5. Top-view SEM images of doped HTM layers.

between adjacent methoxyphenyl and TPASF rings are 3.79 Å and 3.61 Å, respectively (Figure 4c). Furthermore, various intermolecular interactions, including C−H/π, S−H, and hydrogen bonding (F−H), are illustrated in Figure 4d. The observed crystal geometry is consistent with the theoretical calculations discussed earlier.

The surface morphology of HTM layers is critical in determining the photovoltaic performance of PSCs. Scanning electron microscopy (SEM) was performed to assess the surface morphologies of chemically doped HTM layers deposited on the perovskite layer (Figure 5). CPDT- and TTT-based HTMs, which incorporate more planar π-bridge units, exhibited more aggregated films with noticeable voids compared to DTP-and ThOEt-based HTM layers. The presence of these aggregated, non-uniform films likely hinders hole extraction from the perovskite layer, leading to a decline in PSC performance. In contrast, DTP- and ThOEt-based HTMs, despite their similar backbone structures, effectively prevent film aggregation by altering the π-bridge units. These materials produced homogeneous films with fewer pinholes. This indicates that less planar π-bridge units, such as those in DTP and ThOEt, possess an inherent advantage in forming high-quality HTM layers. Such layers help reduce charge-carrier transport losses by minimizing shunting paths and enhancing interfacial contact at the perovskite/HTM layer/electrode interfaces, thereby improving device performance.

To evaluate the impact of our HTMs on photovoltaic performance, we fabricated PSCs with a standard layered architecture: glass/indium tin oxide (ITO; 150 nm)/SnO_2 electron transport layer (30 nm)/perovskite light absorber (650 nm)/HTM layer (~55 nm)/gold electrode (80 nm) (Figure 6a). A triple-cation perovskite with an iodide-rich composition, $Cs_{0.05}(FA_{0.85}MA_{0.15})_{0.95}Pb(I_{0.85}Br_{0.15})_3$, was used as the active layer. The highest PSC performance was achieved when using a precursor solution containing 60 mg/mL of DTP-OFTPASMe2, as shown in Figure S4(a–d) (Supporting Information). Therefore, this concentration was used for fabricating other HTM layers. The current–voltage (*J*–*V*) curves and average device parameters of the as-fabricated PSCs are presented in Figure 6b and Table 2.

Achieving high-performance PSCs requires suitable energy levels, uniform film morphology, and efficient charge transport properties. First, we fabricated devices using CPDT-OFTPASMe2 and TTT-OFTPASMe2 HTMs, both featuring planar backbones. These devices exhibited (day-1) mean PCEs of 8.3% and 8.2%, with *V*oc of 0.77 V and 0.85 V, *J*sc of 22.8 and 22.9 mA cm^{-2}, and FF of 47% and 42%, respectively [see Figure 6(c–f) and Table 2]. The relatively low PCEs can be attributed due to film aggregation, as observed in Figure 5. To mitigate film aggregation, we introduced an alkoxy group in ThOEt-OFTPASMe2 and a methoxy phenyl group in DTP-OFTPASMe2. These modifications resulted in better energy level alignment [Figure 2(c)] and reduced film aggregation (Figure 5), leading to enhanced PSC performance compared to CPDT-OFTPASMe2- and TTT-OFTPASMe2-based devices. ThOEt-OFTPASMe2-based PSCs achieved an PCE of 16.3%, with a *V*oc of 1.00 V, a *J*sc of 23.9 mA cm^{-2}, and an FF of 67%. Even better device performance was observed in DTP-OFTPASMe2-based devices, probably due to smooth layer formation with fewer pinholes, resulting in a *V*oc of 1.07 V, a *J*sc of 24.3 mA cm^{-2}, and an FF of 71%, yielding a PCE of 18.7%. The reference 2,2',7,7'-tetrakis[*N*,*N*-di(4-methoxyphenyl)amino]-9,9'-spirobifluorene (spiro-OMeTAD) device exhibited an average PCE of 20.3%, with a *V*oc of 1.11 V, a *J*sc of 25.0 mA cm^{-2}, and an FF of 73%.

Table 2. Mean photovoltaic parameters and standard deviations of PSCs fabricated using TPASF-based HTMs and spiro-OMeTAD.

HTM	J_{SC} (mA cm^{-2})	V_{OC} (V)	FF	PCE (%)
CPDT-OFTPASMe2	22.8 ± 0.2	0.77 ± 0.02	0.47 ± 0.03	8.3 ± 0.6
TTT-OFTPASMe2	22.9 ± 0.5	0.85 ± 0.03	0.42 ± 0.04	8.2 ± 0.8
ThOEt-OFTPASMe2	23.9 ± 0.3	1.00 ± 0.01	0.67 ± 0.01	16.3 ± 0.2
DTP-OFTPASMe2	24.3 ± 0.3	1.07 ± 0.01	0.71 ± 0.01	18.7 ± 0.1
Spiro-OMeTAD	25.0 ± 0.1	1.11 ± 0.03	0.73 ± 0.01	20.3 ± 0.2

Generally, in a chemical doping process, a charge-transfer reaction occurs from the HTM to the dopant. This reaction oxidizes the HTM, creating additional holes and consequently increasing electrical conductivity. However, in the absence of dopants, HTMs are not oxidized, resulting in poor hole transport properties.[55] In our study, we investigated PSCs with undoped HTM layers. Using undoped CPDT-, TTT-, ThOEt-, and DTP-OFTPASMe2-based HTM layers resulted in mean PCEs of 4.7%, 5.5%, 7.6%, and 4.3%, respectively,

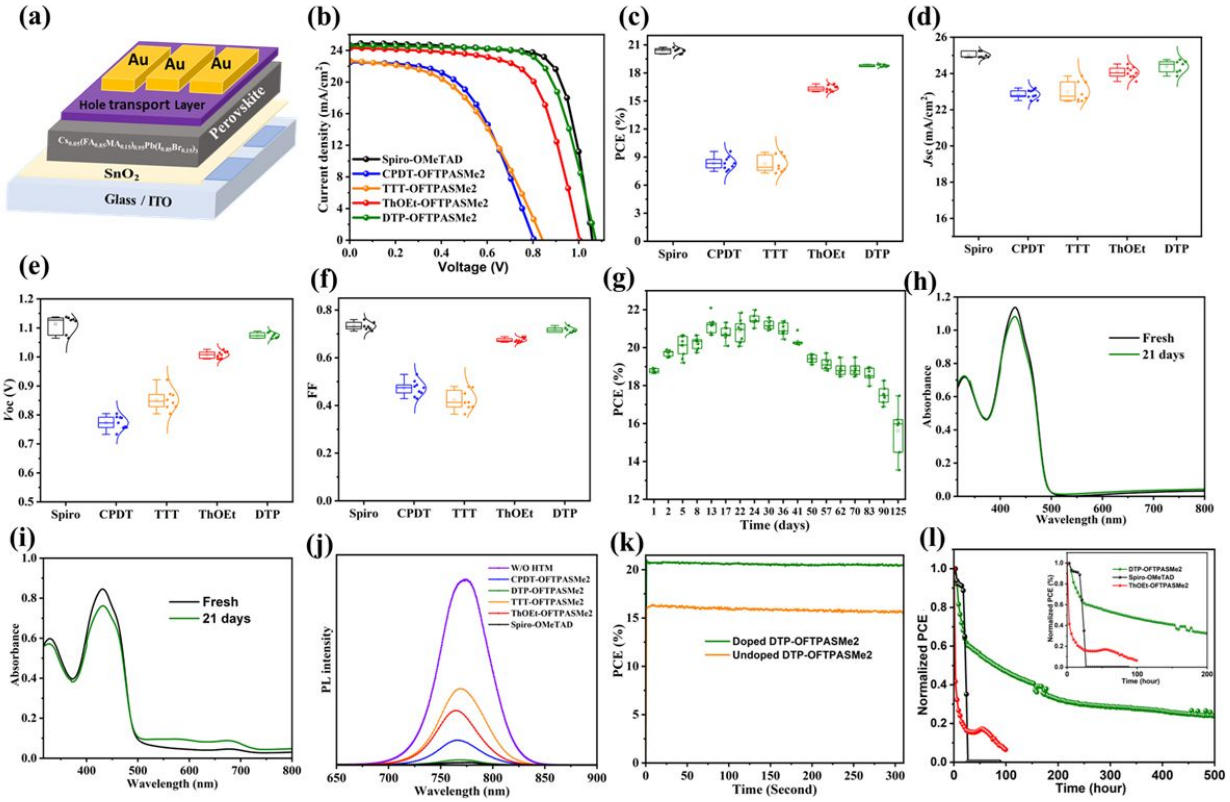

Fig. 6. (a) Schematic diagram of the PSC architecture, (b) *J*–*V* curves of as-fabricated PSCs with chemically doped HTM layers, measured under AM1.5G illumination at 100 mW cm^{-2}, (c–f) Device parameter plots of as-fabricated PSCs. (g) Evolution of device performance for unsealed DTP-OFTPASMe2-based PSCs, showing shelf stability in air at room temperature. UV–VIS-NIR absorption spectra of (h) undoped and (i) chemically doped DTP-OFTPASMe2 thin films before and after 21 days of storage in air. (j) Steady-state PL spectra of the perovskite layer with and without the HTM layer, (k) PCE stabilization of PSCs with undoped and doped DTP-OFTPASMe2 layers, measured using maximum power point tracking, (l) Device operational stability at 85 °C.

with *V*oc of 0.97, 1.09, 1.01, and 1.02 V, *J*sc of 18.0, 22.2, 21.1, and 18.6 mA cm^{-2}, and FF of 27%, 23%, 36%, and 23%, respectively (see Table S3, Supporting Information).

The long-term stability of PSCs is a critical parameter for practical applications. In this study, the shelf stability of CPDT-, TTT-, ThOEt-, and DTP-OFTPASMe$_2$-based PSCs without encapsulation was evaluated under air exposure at a relative humidity of 60 ± 5% (Figure 6g, Figures S5 and S6, Supporting Information). Devices based on CPDT- and TTT-OFTPASMe2 with chemical doping initially showed an increase in PCE due to the improved charge carrier diffusion length of mixed-cation perovskite films[56,57] and oxygen doping, followed by a significant decrease in PCE after 12 days [Figure S6]. This decline in performance is likely due to the penetration of oxygen and water molecules through the non-uniform films formed by these HTM layers, which may damage the perovskite layer. In contrast, the chemically doped ThOEt- and DTP-OFTPASMe2-based HTMs exhibited uniform film formation, which effectively inhibited water molecule penetration, resulting in improved shelf stability. ThOEt-based devices showed a slight increase in PCE after day-2, followed by a gradual decrease in efficiency within 12 days (Figure S6). DTP-based PSCs demonstrated a much slower increase in PCE, rising from average PCE 18.7% to approximately 20% after day-2 of air exposure and maintaining the initial PCE value even after 83 days. For comparison, spiro-OMeTAD devices (with a MoO_3 buffer layer, previously reported by our group) a PCE decrease from approximately 18.25% to 15.28% (~20%) after 25 days of the air storage.[52] The superior shelf stability of DTP-based devices in air (stable for up to 83 days without a MoO_3 layer) can be attributed to several factors: uniform film morphology, defect passivation of the perovskite layer, the hydrophobic nature introduced by F addition, and strong intermolecular interactions in the film state. These characteristics effectively prevent undesirable penetration of air and water, thereby improving the device stability.

We also examined the shelf stability of undoped PSCs without encapsulation under air exposure. The increased carrier diffusion length of perovskite film and the oxygen doping into the HTM layer occurs naturally in the air, leading to a gradual increase in the PCEs of all PSCs over time [Figure S6 and S7(a–d), Supporting Information]. However, the performance of undoped, air-exposed PSCs remained lower than that of chemically doped PSCs, highlighting the limitations of oxygen doping in achieving higher device efficiency.

As discussed earlier, device performance improved during the initial stage of the shelf stability test under air exposure. This enhancement also might be attributed to defect passivation with sulfur atoms of the HTMs, as well as oxygen doping into the HTM layers.[54] To gain further insight into the oxygen doping process, we measured the UV-Vis-NIR absorption spectra of undoped and doped DTP-OFTPASMe2 thin films [Figure 6(h,i)]. In both undoped and

doped DTP films, the π-π* peak intensities at 360 nm changed simultaneously, while the n-π* peak intensities at 420 nm decreased over a period of 21 days. In doped films, the radical cation peak in the 500–800 nm range increased during this period. Compared to doped films, the peak intensities of undoped films remained largely unchanged before and after air exposure, suggesting that oxygen doping was relatively weak, making the radical cation peaks too small to detect. Furthermore, excessive oxygen doping negatively impacted the doped HTL layer. These findings confirm that slow oxygen doping leads to the oxidation of HTM layers, resulting in increased PCE. This effect may stem from an insufficient dopant concentration, which generates an inadequate driving force for hole transfer from the perovskite valence band. Moreover, the trends observed in doped and undoped PSCs with the DTP HTM layer [Figure 6(g), Figure S5(a–c), and Figure S7(a–d)] are consistent with the UV-Vis data presented in Figure 6(h,i).

Additionally, steady-state photoluminescence (PL) spectra were measured to investigate hole extraction properties at the perovskite/doped HTM layer interface [Figure 6(j)]. The results showed that PL intensities decreased more significantly with HTMs that provided higher device performance, indicating more efficient hole extraction from the perovskite layer to the HTM layer. The PL quenching efficiency followed the order: spiro-OMeTAD (98.56%) > DTP-OFTPASMe2 (97.11%) > CPDT-OFTPASMe2 (87%) > ThOEt-OFTPASMe2 (71%) > TTT-OFTPASMe2 (59.5%). The highest PL quenching efficiency observed with the DTP-OFTPASMe2 layer suggests the most efficient hole extraction among the tested materials. Under simulated one-sun illumination, maximum power point tracking was used to evaluate the PCE stabilization. The PCE increased rapidly after illumination began and then stabilized for both undoped and doped PSCs with the DTP-OFTPASMe2 layer measured after 21 days of air exposure [Figure 6(k)]. The stabilized PCE values were consistent with those measured from the *J*–*V* curves.

The primary cause of temperature instability in PSCs is attributed to the HTM layer.[58] In this study, we investigated the high-temperature stability of spiro-OMeTAD based devices as a reference, along with high-performance HTMs i.e., ThOEt-OFTPASMe$_2$ and DTP-OFTPASMe2 by subjecting them to continuous white 3,000 K LED illumination (100 mW cm^{-2}) and heating at 85 °C for up to 147 hours [Figure 6(l)]. We then examined the efficiency variation of the devices over time. Compared to spiro-OMeTAD, PSCs using ThOEt- and DTP-based HTMs exhibited better thermal stability at 85 °C. The spiro-OMeTAD-based device's PCE dropped to 0% within 9 hours, while the ThOEt-based device degraded after approximately 90 hours. In contrast, DTP-based HTM devices retained their functionality 50% until 120 hours and did not completely degrade even after ~500 hours. These results demonstrate that the DTP-OFTPASMe2 HTM offers significantly better high-temperature stability than the reference spiro-OMeTAD. A detailed synthesis cost evaluation of DTP-OFTPASMe2 is presented in Table S4 and S5 (Supporting Information). The cost of the this HTM is approximately one-third that of purified spiro-OMeTAD.

Conclusions

In summary, we designed and synthesized four novel D-π-D structured organic HTMs incorporating bithiophene units as π-bridges linked to a TPASF moiety. TPASF, used as a donor group, has been explored in the field of HTMs for PSCs. The structural differences in the π-bridge units significantly influence optoelectronic properties, molecular packing, device performance, and thermal stability. Strong intermolecular interactions were observed in CPDT- and TTT-OFTPASMe2 HTM films due to the flanked TPASF and fused planar π-bridges, leading to increased void formation. These HTMs exhibited poor efficiency due to the easy penetration of water molecules through the voids, which caused damage to the perovskite active layer. To mitigate strong intermolecular interactions, we introduced ethoxy groups in ThOEt-OFTPASMe2 and methoxyphenyl groups in DTP-OFTPASMe2 HTMs. In DTP-based HTM, the methoxyphenyl unit effectively prevented strong film aggregation, resulting in a pinhole-free morphology. Additionally, the uniform film morphology, hydrophobic nature, and strong intermolecular interactions in the film state helped prevent undesirable air and water penetration. The good energy-level alignment between the DTP-HTM and the perovskite layer enhanced charge extraction while suppressing interfacial recombination. Unsealed DTP-OFTPASMe2-based PSCs demonstrated superior air stability, maintaining over 18.7% efficiency for up to 83 days. Furthermore, the efficiency of DTP-based PSCs increased from 18.7% to 21.35% under ambient conditions due to oxygen doping, as confirmed by UV–VIS absorption spectroscopy. Stability plots further confirmed that DTP-OFTPASMe2 is a more promising HTM compared to the reference spiro-OMeTAD.

Author contributions

T.B.R. conducted the synthesis, device fabrication, evaluation, and data analysis under the supervision of T.M. Gaussian calculations were performed by M.W., and C.A.M.S., Y.F., and D.S. provided support with instrumentation. All authors reviewed and approved the final manuscript.

Conflicts of interest

There are no conflicts to declare.

Data availability

The data that support the findings of this study are available from the corresponding author upon reasonable request.

Acknowledgements

This work was supported by Mitsui Chemicals, Inc.— Carbon Neutral Research Center (MCI-CNRC), I2CNER, Kyushu Univ.; New Energy and Industrial Technology Development Organization (NEDO), the Green Innovation Fund Project (grant number 21578635); Science and Technology Research Partnership for Sustainable Development (SATREPS), Japan Science and Technology Agency (JST) (grant number JPMJSA2306); Precursory Research for Embryonic Science and Technology (PRESTO), JST (grant number JPMJPR23H8); ASPIRE

FOR RISING SCIENTISTS, Adopting Sustainable Partnerships for Innovative Research Ecosystem (ASPIRE), JST (grant number JPMJAP2332); JSPS KAKENHI (grant numbers 20H02817 and 24H00486); the Iketani Science and Technology Foundation; the Murata Science Foundation; the Iwatani Naoji Foundation; and the Asahi Glass Foundation.

References

1 Best Research-Cell Efficiency Chart, 2024. https://www.nrel.gov/pv/cell-efficiency.html. accessed June 4, 2024.

2 C. Liu, Y. Yang, H. Chen, J. Xu, A. Liu, A. S. R Bati, H. Zhu, L. Grater, S. Sudhakar Hadke, C. Huang, V. K. Sangwan, T. Cai, D. Shin, L. X. Chen, M. C. Hersam, C. A. Mirkin, B. Chen, M. G. Kanatzidis and E. H. Sargent, *Science* 2023, **382**, 810–815.

3 Z. Huang, Y. Bai, X. Huang, J. Li, Y. Wu, Y. Chen, K. Li, X. Niu, N. Li, G. Liu, Y. Zhang, H. Zai, Q. Chen, T. Lei, L. Wang and H. Zhou, *Nature*, 2023, **623**, 531–537.

4 Q. Wang, Z. Lin, J. Su, Z. Hu, J. Chang and Y. Hao, *Nano Select*, 2021, **2**, 1055–1080.

5 C. Zhang, K. Wei, J. Hu, X. Cai, G. Du, J. Deng, Z. Luo, X. Zhang, Y. Wang, L. Yang and J. Zhang, *Mat. Today.,* 2023, **67**, 518. DOI: 10.1016/j.mattod.2023.06.009.

6 W. Wang, J. Zhou and W. Tang, *J. Mater. Chem. A,* 2022, **10**, 1150–1178.

7 P. Murugan, T. Hu, X. Hu and Y. Chen, *J. Mater. Chem. A,* 2022, **10**, 5044.

8 C. E. Puerto Galvis, D. A. González Ruiz, E. Martínez-Ferrero and E. Palomares, *Chem. Sci.,* 2023, **15**, 1534.

9 A. Farokhi, H. Shahroosvand, G. D. Monache, M. Pilkington and M. K. Nazeeruddin, *Chem. Soc. Rev.,* 2022, **51**, 5974.

10 X. Yin, Z. Song, Z. Li and W. Tang, *Energy Environ. Sci.*, 2020, **13**, 4057.

11 X. Zhang, X. Liu, F. F. Tirani, B. Ding, J. Chen, G. Rahim, M. Han, K. Zhang, Y. Zhou, H. Quan, B. Li, W. Du, K. G. Brooks, S. Dai, Z. Fei, A. M. Asiri, P. J. Dyson, M. K. Nazeeruddin and Y. Ding, *Angew. Chem*, 2024, **63**, 202320152.

12 Z. Yao, F. Zhang, L. He, X. Bi, Y. Guo, Y. Guo, L. Wang, X. Wan, Y. Chen and L. Sun, *Angew. Chem.*, 2022, **61**, 202201847.

13 Y. Hua, S. Chen, D. Zhang, P. Xu, A. Sun, Y. Ou, T. Wu, H. Sun, B. Cui and X. Zhu, *J. Mater. Chem. A,* 2019, **7**, 10200–10205.

14 L. Yuan, W. Zhu, Y. Zhang, Y. Li, C. C. S. Chan, M. Qin, J. Qiu, K. Zhang, J. Huang, J. Wang, H. Luo, Z. Zhang, R. Chen, W. Liang, Q. Wei, K. S. Wong, X. Lu, N. Li, C. J. Brabec, L. Ding and K. Yan, *Energy Environ. Sci.*, 2023, **16**, 1597–1609.

15 H. D. Pham, T. T. Do, J. Kim, C. Charbonneau, S. Manzhos, K. Feron, W. C. Tsoi, J. R. Durrant, S. M. Jain and P. Sonar, *Adv. Energy Mater.*, 2018, **8**, 1703007.

16 C. Shen, Y. Wu, H. Zhang, E. Li, W. Zhang, X. Xu, W. Wu, H. Tian and W. Zhu, *Angew. Chemie.*, 2019, **131**, 3824–3829.

17 D. E. M. Rojas, K. T. Cho, Y. Zhang, M. Urbani, N. Tabet, G. de la Torre, M. K. Nazeeruddin and T. Torres, *Adv. Energy Mater.*, 2018, **8**, 1800681.

18 Z. Dong, X. Yin, A. Ali, J. Zhou, S. S. Bista, C. Chen, Y. Yan and W. Tang, *J. Mater. Chem. C,* 2019, **7**, 9455–9459.

19 S. Mabrouk, M. Zhang, Z. Wang, M. Liang, B. Bahrami, Y. Wu, J. Wu, Q. Qiao and S. Yang, *J. Mater. Chem. A,* 2018, **6**, 7950–7958.

20 R. Sandoval-Torrientes, I. Zimmermann, J. Calbo, J. Aragó, J. Santos, E. Ortí, N. Martín and M. K. Nazeeruddin, *J. Mater. Chem. A,* 2018, **6**, 5944–5951.

21 J. Zhou, X. Yin, Z. Dong, A. Ali, Z. Song, N. Shrestha, S. S. Bista, Q. Bao, R. J. Ellingson, Y. Yan and W. Tang, *Angew. Chem.*, 2019, **131**, 13855–13859.

22 A. Zheng, J. Wang, N. Xu, R. Zhu, Y. Yuan, J. Zhang, J. Zhang, Z. Li and P. Wang, *ACS Photonics*, 2018, **5**, 4694–4701.

23 Y. Ren, Y. Cai, L. He, A. Zheng, Y. Yuan, J. Zhang and P. Wang, *ACS Mater. Lett.*, 2022, **4**, 600–608.

24 C. Lorenz, A. Vogt, J. Millan, E. Mena-Osteritz and P. Bäuerle, *Organic Materials*, 2022, **5**, 35–47.

25 Z. Wang, S. Yan, Z. Yang, Y. Zou, J. Chen, C. Xu, P. Mao, S. Ding, J. Chen, X. Zong, T. Qin and M. Liang, *Chem. Eng. J.*, 2022, **450**, 138189.

26 Q. Cheng, H. Chen, W. Chen, J. Ding, Z. Chen, Y. Shen, X. Wu, Y. Wu, Y. Li and Y. Li, *Angew. Chemie.,* 2023, **62**, e202312231.

27 I. García-Benito, I. Zimmermann, J. Urieta-Mora, J. Aragó, A. Molina-Ontoria, E. Ortí, N. Martín and M. K. Nazeeruddin, *J. Mater. Chem. A,* 2017, **5**, 8317–8324.

28 Y. Ou, A. Sun, H. Li, T. Wu, D. Zhang, P. Xu, R. Zhao, L. Zhu, R. Wang, B. Xu, Y. Hua and L. Ding, *Mater. Chem. Front.*, 2021, **5**, 876–884.

29 J. Y. Shao, N. Yang, W. Guo, B. Bin Cui, Q. Chen and Y. W. Zhong, *Chem. Com.*, 2019, **55**, 13406–13409.

30 H. Guo, H. Zhang, C. Shen, D. Zhang, S. Liu, Y. Wu and W. H. Zhu, *Angew. Chemie.,* 2021, **60**, 2674–2679.

31 Y. J. Chang, N. H. Chen, T. Y. Chen, Y. M. Shuang and Y. S. Yen, *ACS Appl. Energy Mater.*, 2024, **7**, 1287–1297.

32 B. X. Zhao, C. Yao, K. Gu, T. Liu, Y. Xia and Y. L. Loo, *Energy Environ. Sci.*, 2020, **13**, 4334–4343.

33 R. Li, J. Zhang, M. Liu, S. K. Matta, J. Tian, Z. Deng, S. P. Russo, P. Vivo, Z. Zhou and H. Zhang, *Sol. RRL.*, 2023, **7**, 2300031.

34 M. Li, J. Wu, G. Wang, B. Wu, Z. Sun, S. Xue, Q. Qiao and M. Liang, *J. Eng. Chem.*, 2020, **47**, 10–17.

35 J. Wang, H. Zhang, B. Wu, Z. Wang, Z. Sun, S. Xue, Y. Wu, A. Hagfeldt and M. Liang, *Angew. Chemie.*, 2019, **131**, 15868–15872.

36 X. Zhang, S. Zhang, X. Liao, B. Ding, G. Rahim, K. Zhao, J. Chen, M. Han, Y. Zhou, P. Shi, K. Zhang, S. Kinge, H. Zhang, R. Wang, K. G. Brooks, S. Dai, X. Liu, Z. Fei, P. J. Dyson, M. K. Nazeeruddin and Y. Ding, *Adv. Funct. Mater.*, 2024, **34**, 2314086.

37 V. Kumar, D. Kumar, R. D. Chavan, K. P. Kumar, B. Yadagiri, M. Ans, J. Kruszyńska, A. Mahapatra, J. Nawrocki, K. Nikiforow, N. Mrkyvkova, P. Siffalovic, P. Yadav, S. Akin, S. P. Singh and D. Prochowicz, *J. Mat. Chem. A,* 2024, **12**, 8370–8380.

38 K. Jiang, J. Wang, F. Wu, Q. Xue, Q. Yao, J. Zhang, Y. Chen, G. Zhang, Z. Zhu, H. Yan, L. Zhu and H. L. Yip, *Adv. Mat.*, 2020, **32**, 1908011.

39 C. Zhou, X. Xu, Z. Liu, Z. Sun, Z. Chen, X. Chen, L. Chen, X. Fang, J. Zhang, Y. M. Yang, X. Jia, N. Yuan and J. Ding, *ACS Appl. Mat. Interfaces*, 2023, **15**, 22752–22761.

40 H. Yao, T. Wu, B. Wu, H. Zhang, Z. Wang, Z. Sun, S. Xue, Y. Hua and M. Liang, *J. Mater. Chem. A,* 2021, **9**, 8598–8606.

41 X. Zhang, X. Liu, N. Wu, R. Ghadari, M. Han, Y. Wang, Y. Ding, M. Cai, Z. Qu and S. Dai, *J. Eng. Chem.*, 2022, **67**, 19–26.

42 G. B. Adugna, K. M. Lee, H. C. Hsieh, S. I. Lu, C. H. Lin, Y. C. Hsieh, J. H. Yang, J. M. Chiu, Y. S. Liu, C. W. Hu, W. H. Chiu, S. R. Li, K. L. Liau, Y. T. Tao and Y. D. Lin, *Sol. RRL.*, 2024, **8**, 2300988.

43 G. B. Adugna, K. M. Lee, H. C. Hsieh, S. I. Lu, Y. C. Hsieh, J. H. Yang, W. H. Chiu, K. L. Liau, Y. T. Tao and Y. D. Lin, *Chem. Comm.*, 2023, **59**, 14653–14656.

44 Z. Zhang, L. Shen, S. Wang, L. Zheng, D. Li, Z. Li, Y. Xing, K. Guo, L. Xie and Z. Wei, *Adv. Energy Mater.*, 2023, **13**, 2204362.

45 M. Jeong, I. Woo Choi, E. Min Go, Y. Cho, M. Kim, B. Lee, S. Jeong, Y. Jo, H. Won Choi, J. Lee, J.-H. Bae, S. Kyu Kwak, D. Suk Kim and C. Yang, Science, 2020, **369**, 1615–1620.

46 X. Yin, C. Wang, D. Zhao, N. Shrestha, C. R. Grice, L. Guan, Z. Song, C. Chen, C. Li, G. Chi, B. Zhou, J. Yu, Z. Zhang, R. J. Ellingson, J. Zhou, Y. Yan and W. Tang, *Nano Energy*, 2018, **51**, 680–687.

47 G. M. Kim, H. Sato, Y. Ohkura, A. Ishii and T. Miyasaka, *Adv. Energy Mater.*, 2022, **12**, 2102856.

48 J. Yang, J. Huang, C. Zhang, H. Sun, B. Li, Y. Wang, K. Feng, Q. Liao, Q. Bai, L. Niu, H. Wang and X. Guo, *Adv. Funct. Mater.*, 2022, **32**, 2206311.

49 K. M. Lee, C. H. Lin, C. C. Chang, T. Y. Yang, W. H. Chiu, W. C. Chu, Y. H. Chang, S. R. Li, S. I. Lu, H. C. Hsieh, K. L. Liau, C. H. Hu, C. H. Chen, Y. S. Liu, W. C. Chou, M. M. Lee, S. S. Sun, Y. T. Tao and Y. D. Lin, *Adv. Sci*. 2025, **12**, 2410666.

50 K. M. Lee, Y. S. Huang, W. H. Chiu, Y. K. Huang, G. Chen, G. B. Adugna, S. R. Li, F. J. Lin, S. I. Lu, H. C. Hsieh, K. L. Liau, C. C. Huang, Y. Tai, Y. T. Tao and Y. D. Lin, *Adv. Funct. Mater.* 2023, **33**, 2306367.

51 K. Yang, Q. Liao, J. Huang, Z. Zhang, M. Su, Z. Chen, Z. Wu, D. Wang, Z. Lai, H. Y. Woo, Y. Cao, P. Gao and X. Guo, *Angew. Chem.,* 2022, **61**, e202113749.

52 Y. D. Lin, S. Y. Abate, H. C. Chung, K. L. Liau, Y. T. Tao, T. J. Chow and S. S. Sun, *ACS Appl. Energy Mater.*, 2019, **2**, 7070–7082.

53 G. Tumen-Ulzii, M. Auffray, D. Klotz, G. F. Harrington, X. K. Chen, U. Balijapalli, V. Vediyappan, N. Nakamura, Z. Feng, K. Takekuma, Y. Fujita, P. Wang, S. Yamada, K. Tamada, M. Batmunkh, Y. L. Zhong, F. Mathevet, H. Salway, M. Anaya, S. D. Stranks, T. Matsushima and C. Adachi, *ACS Appl. Energy Mater.*, 2022, **5**, 15819–15827.

54 B. Purev-Ochir, X. Liu, Y. Fujita, D. Semba, T. B. Raju, G. Tumen-Ulzii, A. Wachi, H. Sato, T. Matsushima and C. Adachi, *Sol. RRL.*, 2023, **7**, 2300127.

55 W. Zhou, Z. Wen and P. Gao, *Adv. Energy Mater.,* 2018, **8**, 1702512.

56 M. Ozaki, Y. Ishikura, M. A. Truong, J. Liu, I. Okada, T. Tanabe, S. Sekimoto, T. Ohtsuki, Y. Murata, R. Murdey and A. Wakamiya, *J. Mater. Chem. A,* 2019, **7**, 16947–16953.

57 Y. Cho, H. Do Kim, J. Zheng, J. Bing, Y. Li, M. Zhang, M. A. Green, A. Wakamiya, S. Huang, H. Ohkita and A. W. Y. Ho-Baillie, *ACS Energy Lett.*, 2021, **6**, 925–933.

58 H. Zheng, G. Liu, C. Zhang, L. Zhu, A. Alsaedi, T. Hayat, X. Pan and S. Dai, *Sol. Energy*, 2018, **159**, 914–919.

The data that support the findings of this study are available from the corresponding author upon reasonable request.